RESEARCH

Oxygen transport in nanoporous SiN membrane compared to PDMS and polypropylene for microfluidic ECMO

Nayeem Imtiaz[1] · William A. Stoddard[1] · Abdelrahman Ghazy[1] · Steven W. Day[1]

Abstract

Extracorporeal Membrane Oxygenation (ECMO) serves as a crucial intervention for patients with severe pulmonary dysfunction by facilitating oxygenation and carbon dioxide removal. While traditional ECMO systems are effective, their large priming volumes and significant blood-contacting surface areas can lead to complications, particularly in neonates and pediatric patients. Microfluidic ECMO systems offer a promising alternative by miniaturizing the ECMO technology, reducing blood volume requirements, and minimizing device surface area to improve safety and efficiency. This study investigates the oxygen transport performance of three membrane types— polydimethylsiloxane (PDMS), polypropylene, and a novel nanoporous silicon nitride (NPSiN) membrane—in a microfluidic ECMO platform. While nanoporous membranes rely on pore-mediated diffusion and PDMS on polymer lattice diffusion, results show no significant differences in device oxygenation efficiency ($p > 0.05$). Blood-side factors, including the diffusion rate of oxygen through the red blood cell (RBC) membrane, RBC residence time, and hemoglobin binding kinetics, were identified as primary bottlenecks. Even computational models of a hypothetical infinitely permeable membrane corroborate the limited impact of membrane material. These findings suggest a shift in ECMO design priorities from membrane material to blood-side enhancements. This research provides a foundation for optimizing ECMO systems.

Keywords Microfluidic ECMO · Nanoporous SiN · Oxygen transport · Membrane permeability · Blood-side limitations

1 Introduction

The prevalence in chronic lung diseases, such as Chronic Obstructive Pulmonary Disease (COPD), along with sudden outbreaks of infectious diseases like swine flu and COVID-19, has highlighted the need for better treatments for respiratory insufficiency and respiratory failure (Berlin et al. 2020; Roberts et al. 2024). Mechanical ventilation is the standard treatment, but it involves invasive procedures

that carry serious risks, such as barotrauma, ventilator-associated pneumonia, and other infections (Fan et al. 2017). In response, Extracorporeal Membrane Oxygenation (ECMO) has become increasingly significant. ECMO is a technique that circulates blood through an external circuit to allow gas exchange in an artificial lung, which can help reduce or, in some cases, avoid the need for a ventilator (Auld et al. 2020; Li et al. 2020). Although ECMO has become safer and more effective over the past 20 years, there are still important areas that need improvement. Patients on ECMO are at risk for several complications, including infection, thrombosis, embolism, and hemorrhage (Aubron et al. 2013).

Microfluidic-based ECMO devices have the potential to transform ECMO treatment by significantly reducing blood volume, blood-contacting surface area, and overall device size. This reduction in blood volume benefits patients of all ages and is especially crucial for smaller patients, such as neonates. Additionally, minimizing the membrane and device surface area, lowers the risk of complications and reduces blood damage (Dabaghi et al. 2018a; Rode et al. 2020). Current oxygenators usually have a tube-in-tube

✉ Steven W. Day
  swdeme@rit.edu

  Nayeem Imtiaz
  nayeemimtiaz1993@gmail.com

  William A. Stoddard
  stoddawa@mail.uc.edu

  Abdelrahman Ghazy
  amg7121@rit.edu

[1] Rochester Institute of Technology, Kate Gleason College of Engineering, Rochester, NY 14623, USA

design (Odish et al. 2023; Shin et al. 2024), whereas many microfluidic devices, such as lab-on-a-chip systems, are arranged in stacked planar layers (Abudupataer et al. 2020; Hou et al. 2018). This stacked configuration is compatible with a new generation of ultra-high permeability membranes that are manufactured on a wafer and must remain planar (Dabaghi et al. 2018a; Rode et al. 2020).

Various groups have made significant progress in the development of microfluidic oxygenators over the past decade, using advances in computational designs, microfabrication techniques, and biomaterials technologies to create prototype devices that have been tested in vitro and in numerous proof of concept studies (Abada et al. 2018; Burgess et al. 2009; Dabaghi et al. 2018b; Imtiaz et al. 2022, 2023a, b).

Regardless of great advancements in microfluidic ECMO research, challenges still remain in reducing priming volume and membrane surface area, particularly for neonatal and pediatric applications. Developing advanced membrane and device technologies to create miniaturized ECMO systems with lower priming volumes is therefore essential. The majority of devices in the literature utilize PDMS as the membrane material (Dabaghi et al. 2019; Ma et al. 2022; Potkay 2014; Santos et al. 2021), leaving the potential benefits of more advanced, novel membrane materials largely unexplored. It has been proposed that using a high gas-permeant membranes enable greater oxygen transfer across the membrane surface, which could result in more efficient oxygen delivery over time (Gimbel et al. 2021), eventually resulting in reduced device size.

To miniaturize the microfluidic ECMO it is important to select a membrane with high gas permeance. High gas-permeant membranes enable greater oxygen transfer across the membrane surface, which could result in more efficient oxygen delivery over time (Gimbel et al. 2021). PDMS membranes used in current microfluidic ECMO devices offer limited gas-permeance. Conventional ECMOs, on the other hand, typically employ polypropylene membranes (Valenzuela-Faccini et al. 2024), which, while more permeable than PDMS, are still not a substantial improvement (Table 1) (Ariyoshi et al. 2021; Chui et al. 2022).

Nanomembranes, which consist of nano sized holes patterned into an otherwise impermeable material, hold significant promise for transforming a wide range of fields, including separation processes, energy production, medical applications (Blauvelt et al. 2023; Conlisk et al. 2009; Desai et al. 1999; Gimi et al. 2009; Han et al. 2008a; Haque et al. 2013; Jeon et al. 2012; Kim et al. 2008; Qi et al. 2014; Siwy et al. 2005; Snyder et al. 2011). Commonly fabricated from silicon nitride (SiN) material, these membranes have since been utilized in numerous applications, such as cell culture, electro-osmotic pumping, hemodialysis, lab-on-a-chip devices, and investigations into portable hemodialysis systems (Han et al. 2008b; Hill et al. 2020; Stroeve and Ileri 2011). SiN is a robust, thin ceramic material used in microfabrication due to its mechanical strength and chemical stability. The permeability of nanoporous silicon nitride (NPSiN) is not only three orders of magnitude higher than that of polydimethylsiloxane (PDMS), but also, due to its ultrathin nature (<500 nm), the gas-permeance of the NPSiN membrane is five orders of magnitude higher than PDMS (Formica et al. 2008; Miller et al. 2020). The membrane thickness, gas permeance, permeability, and membrane resistance values for the membranes investigated in this study are summarized in Table 1. Permeability (P) is an intrinsic membrane property, gas permeance (P_m) is Permeability divided by membrane thickness (L), $P_m = P/L$, membrane resistance (R_m) is proportional to membrane thickness and inversely proportional to permeability, $R_m = L/P$.

Despite the potential of NPSiN as an ultra-high permeability membrane, a comparative analysis of different membrane materials within a standardized device platform remains largely unexplored. NPSiN membranes could offer a promising alternative for micro ECMO applications due to their unique properties (Miller et al. 2020). In this study, we investigate the oxygen transport performance of three distinct membrane materials—nanoporous SiN, PDMS, and polypropylene—within a prototype modular microfluidic ECMO device platform (Fig. 1a), using both empirical methods and computational fluid dynamics (CFD) simulations. This comparative analysis is designed to evaluate the efficacy of NPSiN as a novel membrane material. Additionally, we include a hypothetical model of an infinitely permeable membrane to represent an ideal scenario for oxygen transport. This work aims to provide the medical device community with deeper insights into the impact of

Table 1 Membrane thickness, gas permeance, permeability, and membrane resistance information for the nanoporous sin, PDMS, and polypropylene membrane

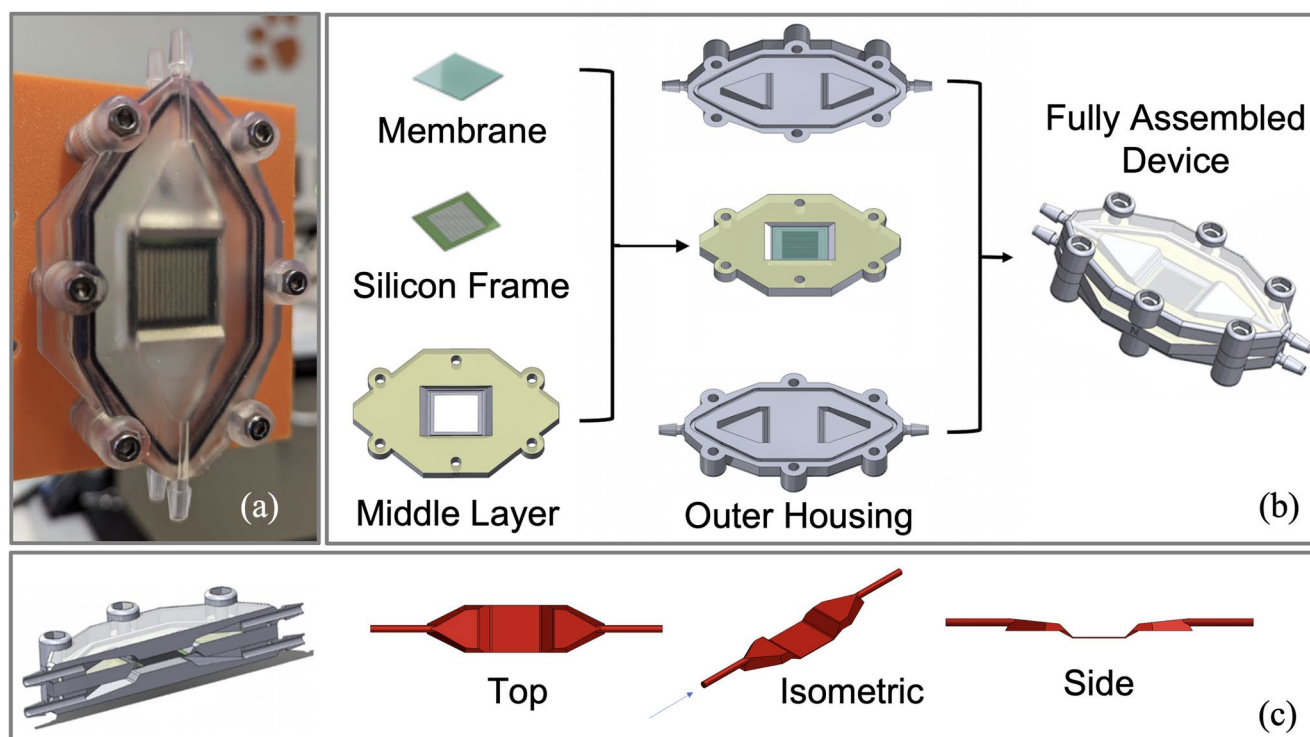| Membrane Material	Permeability (P)		Membrane Thickness (L)	Gas Permeance (P_m)		Membrane Resistance (R_m)	
	(cc·cm·min^{-1}·bar^{-1}·cm^{-2})	m^2/(s·Pa)	(μm)	(cc·min^{-1}·bar^{-1}·cm^{-2})	m/(s·Pa)	(min·bar·cm^{-1})	(s/m)·Pa
Nanoporous SiN	0.54	9.0×10^{-12}	0.4	13,500	2.3×10^{-5}	7.4×10^{-5}	44,400
PDMS	2.7×10^{-3}	4.5×10^{-14}	20	1.4	2.3×10^{-9}	0.72	4.3×10^{8}
Polypropylene	76.5	1.3×10^{-9}	170	4500	7.6×10^{-6}	2.2×10^{-4}	132,000

Fig. 1 a) Modular microfluidic ECMO test device prototype, **b**) Full device assembly, with two outer housings and middle layer. **c**) Blood flow path in the blood side of the device

Table 2 Geometrical features of the prototype ECMO device

Property	Dimension
Inlet port inner diameter (mm)	2.6
Outlet port inner diameter (mm)	2.6
Device length (inlet to outlet) (cm)	10.6
Channel height (mm)	0.4
Active membrane area (cm^2)	1.77
Device volume (cm^3)	1.73

membrane material selection in the design of microfluidic ECMO systems and blood-gas exchangers in general.

2 Materials and methods

2.1 Membranes

The NPSiN membrane, with a thickness of 400 nm, 20% porosity, and 500 nm pore size, was obtained from SiMPore (NY, USA) (Hill et al. 2020). 20 μm thick PDMS membranes used in this study was also obtained from SiMPore, USA. The polypropylene membrane (Sterlitech (WA, USA), had a thickness of 170 μm and nominal pore sizes of 200 nm.

2.2 Device design and fabrication

The microfluidic ECMO device prototypes were designed using SolidWorks 2020, and fabricated through 3D printing using a Form 3+SLA printer (Formlabs) and biocompatible resin (BioMed Clear Resin). The device consists of two outer housings, a middle layer, and a membrane (Fig. 1b). A silicon frame was used to support the PDMS and polypropylene membranes, and frames were attached to the device's middle layer with PDMS adhesive (Fig. 1b). The NPSiN was sourced with the same silicon support frame as used for the PDMS and polypropylene membranes. After membrane attachment, the middle layer is sandwiched between two outer housings (Fig. 1b). The final assembly is the full microfluidic ECMO device prototype. The modular nature of the ECMO prototype allows for rapid exchange of the membrane layer. Figure 1c shows the blood flow path through the blood side of the device. Table 2 shows the device dimensions in detail.

2.3 Experimental setup

The experimental setup is illustrated in Fig. 2a and b. One SpO₂ sensors (CritLine, USA) were placed at the outlet of the blood side of the device, to monitor oxygenation levels. The Critline SpO_2 directly reported saturated blood oxygen
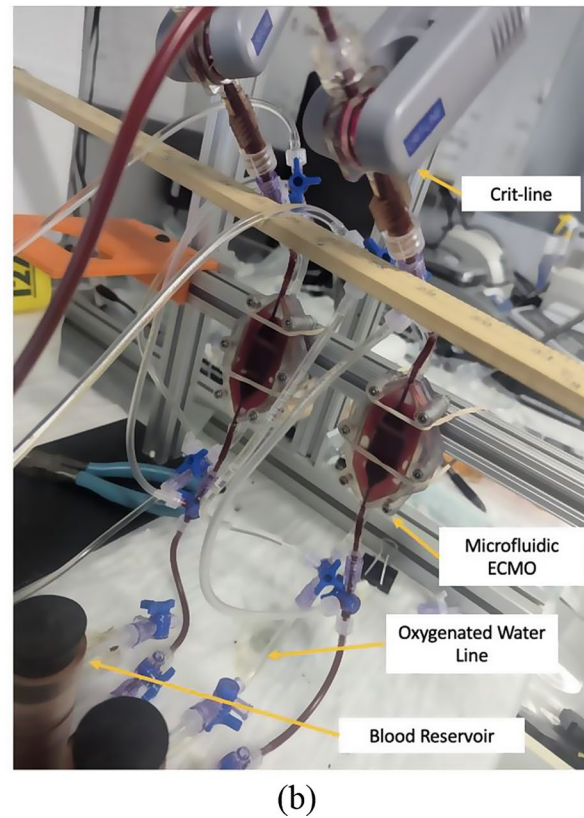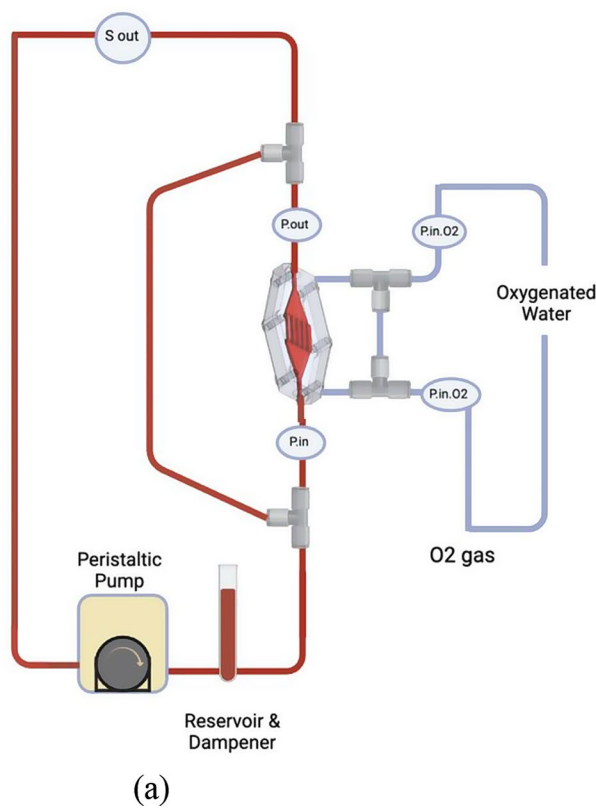
Fig. 2 Oxygen transport in the blood through oxygenated water experimental setup (**a**) schematic diagram and (**b**) setup image

level percentage. From the ΔSpO_2 the ΔO_2 (ml) was calculated using Eq. 1. Where, ΔO_2, V_{blood}, Hb, and ΔSpO_2 are oxygen gain (ml of O_2), volume of blood (dl), hemoglobin concentration (g/dl), and change in oxygen saturation (in %) respectively. The pressure drop between the inlet and outlet of the blood side was monitored. O_2-saturated water was flowed at 8 ml/min on the gas side of the device. A peristaltic pump was used to recirculate blood through the loop, while a custom-designed blood reservoir served as both a reservoir and a dampener. To eliminate atmospheric gas interference with the blood, a custom-designed reservoir was developed featuring a "floating boat lid" (Fig. S2). This lid is designed to rest directly on the fluid surface within the reservoir, thereby minimizing any headspace and reducing the blood's exposure to atmospheric gases. By keeping the blood surface effectively sealed, the floating lid helps ensure more accurate measurements of oxygen transport by limiting unintended oxygen transfer from the environment.

$$\Delta O_2\,(ml) = V_{blood} \times \left(\frac{Hb \,\times\, 1.34 \,\times\, \Delta SpO_2}{100} \right) \tag{1}$$

To quantify oxygen transfer in a flow-independent manner, we report oxygenation performance in terms of "per-pass" oxygen gain, which refers to the amount of oxygen added to

the blood as it passes once through the ECMO device. This metric enables direct comparison across different membrane types and flow rates, independent of how much blood is processed per unit time. Reporting SpO$_2$% rise per-pass and O$_2$ (ml) gain per-pass isolates the efficiency of a single blood circulation through the device and provides a standardized measure of membrane performance that is not confounded by differences in flow rate.

To confirm that the observed oxygen transport was solely due to the gas-permeable membranes and not from external contamination or system artifacts, a negative control experiment was performed using a non-permeable "dummy" membrane under identical flow and environmental conditions. As expected, this setup resulted in no measurable change in oxygen content across the device. This control reinforces that all oxygen transfer observed in the tested devices was indeed attributable to the gas-permeable properties of the membranes used (PDMS, SiN, and polypropylene).

2.3.1 Rationale for using oxygenated water instead of pure oxygen gas

The NPSiN membrane is highly fragile, and exposure to pure oxygen gas on the gas side led to membrane failure, preventing the completion of experiments. To address this

issue, oxygenated water was used as an alternative to pure oxygen gas. This approach provided a stable oxygen source without compromising membrane integrity, allowing the NPSiN membranes to remain intact throughout the experimental process.

Heparinized bovine calf blood (Lampire, USA) was reduced to an initial SpO₂ of 70% by bubbling the blood with nitrogen. A volume of 30 mL of prepared blood was then loaded into the continuous flow loop. Oxygen gain was measured and reported as SpO₂% increase per pass, SpO₂% increase per minute, mL O₂ gain per pass, and mL O₂ gain per minute. For each flow rate (0.2, 0.5, 1, and 2 mL/min) and membrane type, 4 to 6 samples ($n = 3$–6) were taken to ensure statistical robustness. The flow rate of the oxygenated water was 8 ml/min.

2.3.2 Blood viability assessment

A pre-experiment screening was conducted to ensure blood viability. In this assessment, the blood was bubbled with oxygen. Only blood that demonstrated an SpO₂ increase of at least 2% per minute in a 100 mL sample was considered viable.

2.4 Computational model setup

Our setup consisted of a device that flows blood through a channel adjacent to a membrane, with a second channel on the other side of the membrane, carrying oxygenated water. The geometry was generated from the files used to create the 3D-printed test article. The geometry for the flow path was imported to ANSYS Workbench 2020 for meshing. A hexahedral mesh was generated with refinements around areas of geometrical complexity. The highest refinement was in the section adjacent to the membrane. It had a target cell size of 0.04 mm. An inflation region at the membrane wall was implemented to capture the diffusion boundary layer accurately. The inflation zone is 10 cells thick, with a ratio of 1.2 per layer, resulting in the smallest cell height being 6 nm. The resulting mesh is 7.26 million nodes. Fig. S1 shows the Flowchart of the computational model for membrane oxygen transport.

The mesh was then imported into ANSYS Fluent 2020. Using computational fluid dynamics (CFD), ANSYS Fluent enables researchers to model complex blood flow behavior, including velocity profiles, shear stress, and pressure distributions within medical devices and blood vessels (Imtiaz et al. 2024; Nayeem Imtiaz and Tasfia Siam 2023). A steady laminar flow solver was used to calculate the velocity field and transport. The oxygen transfer was simulated using a modified User Defined Function (UDF) code that originally simulated dialysis. The oxygen transport term was defined

as a species and their transport was governed by the blood or dialysate flow fields. The oxygen-saturated water computational domain was mathematically coupled to the blood domain through the UDF architecture to implement source/sink and convective terms across the membrane, thus allowing species to move across the membrane.

The user-defined variable is in units of mg/L of O2. The concentration calculated for 70% saturation in human blood is entered as the blood side inlet. This matches the 70% oxygenation done in our bovine blood experiments for validation. The inlet for the oxygenated water side is initiated at 100% saturation for 1 atmosphere of O2. Henry's law is used to calculate the concentration of oxygen in water (in mg/L) in the water side. Fick's first law (Eq. 1) gives the diffusion across the membrane. The flux J_i through an adjacent cell pair i at the membrane is calculated for each timestep, where D_m represents the calculated membrane diffusivity and ΔC is the concentration gradient across the paired cells.

$$J_i = D_m \Delta C \tag{2}$$

In order to account for the plasma oxygen concentration, a combination of the Hill Equation (Eq. 3) (Hill 1910) and Henry's law for plasma are used to get a relationship between total blood oxygen content and the plasma concentration (Sové et al. 2016). An average hematocrit was chosen in the normal human range (Walker 1990). In Hill's law (Eq. 3), SO2 is the hemoglobin oxygen saturation, N is the Hill coefficient, PO2 is oxygen partial pressure and P50 is the partial pressure of oxygen at 50% saturation. The equations are not simple to solve, so a 3rd order polynomial trendline is used in the calculation as an approximation. The diffusivity of oxygen through a 20 μm PDMS membrane was compared to a NPSiN chip with cylindrical pores (Wright et al. 2020). The membrane resistance, which is the inverse of membrane permeability, was used in the model to dictate membrane properties (Table 1). Given an initial oxygen partial pressure difference (ΔP) of 120 mmHg, with the oxygenated water side at 100% O₂ saturation and the blood side at 70% O₂ saturation, the calculated membrane resistance was 2.78 s/m for NPSiN and 2688 s/m for PDMS. Additionally, a hypothetical infinitely permeable membrane (zero membrane resistance) was modeled to provide a "best-case scenario" and was compared to the PDMS and NPSiN membrane.

$$SO_2 = \frac{PO_2^N}{P_{50}^N + PO_2^N} \tag{3}$$

The mass flow of the blood is set for each case in the UDF, and a parabolic velocity profile is assigned to the inlet. The water flow is kept at a constant 8 ml/min to mimic the set-up

of the experiment. Once the simulation has converged, a mass average of the outlet concentration of O2 is obtained. The initial concentration of O2 in plasma is subtracted from the outlet concentration. This results in the total concentration in mg/L that was transmitted into the blood. This is added to the 70% saturation total oxygen level of whole blood, including oxygen in the hemoglobin. This is divided into the carrying capacity for the hemoglobin in blood to get the outlet saturation, SO2.

2.5 Data analysis

The cross-membrane and cross-flow rate comparison for the empirical experiments was done using the one-way analysis of variance (ANOVA), where $p < 0.05$ indicates that two sets of data are distinct. The computational and empirical data for the membranes were compared by one-sample t-test, where a $p < 0.05$ indicates that the computational datum is distinct from the empirical data. Software tool Graphpad Prism 10 was used for data post-processing and statistics.

3 Results

3.1 Empirical results

Figure 3a and b presents the oxygen transport performance of the three membrane types across four flow rates. Figure 3a illustrates the $SpO_2\%$ increase and O_2 (ml) gain per pass for each membrane type as the full blood volume flows through the device. Results indicate that at any given flow rate, the O_2 increase is not significantly different between membrane types ($p > 0.05$), where it is evident that per-pass oxygen transport decreases for all membranes as the flow rate increases. Figure 3b display the $SpO_2\%$ increase and O_2 (ml) gain per minute. These data reveal that oxygen gain per minute does not differ significantly between membrane types at a given flow rate, and it increases for all membranes as the flow rate increases. The pressure drops between the inlet and outlet of the blood side remained within 0.03 to 0.2 PSI for all flow rates.

3.2 Empirical vs. Simulation

Figure 3c and d shows the oxygen transport comparison between the empirical and simulation data for PDMS and NPSiN membrane. It is observed that for all flow rates the empirical agrees with the simulation results ($p > 0.05$), indicating that the simulation model was successful in predicting the oxygen transport. The oxygen transport behavior observed for the empirical described in Fig. 3a and b holds true for the simulations.

3.3 Hypothetical infinite permeability membrane (simulation)

Figure 3e and f shows the computational oxygen transport values for the hypothetical infinite permeability membrane compared to the NPSiN and PDMS simulations. The results indicate that the oxygen gain with the hypothetical perfect membrane is slightly higher than with the conventional membranes, but the increase is minimal.

4 Discussion

In the NPSiN and polypropylene membranes, oxygen transport occurs through a pore-mediated diffusion mechanism. Unlike non-porous PDMS membranes, where gas molecules must diffuse through the solid material, these membranes contain micro- or nano-sized pores that allow oxygen to enter and fill the pore spaces directly. Oxygen molecules then diffuse through these pores without interacting with the membrane material itself. Upon reaching the blood side of the ECMO system, oxygen exits the pores and diffuses directly into the blood. This pore-centric approach enables efficient gas transfer, as the pathway for oxygen diffusion is governed by the pore architecture rather than by the intrinsic diffusivity of the membrane material. In contrast, the PDMS membrane lacks such pores, so oxygen must diffuse directly through the membrane material itself. This happens as oxygen molecules diffuse through the polymer matrix of PDMS by passing through the interconnected network of polymer chains. This occurs because PDMS is an amorphous polymer with a flexible and loosely packed molecular structure. The polymer chains create regions of free volume within the material, allowing small gas molecules, such as oxygen, to diffuse through governed by the concentration gradient across the membrane. The diffusion in PDMS is thus slower, as it depends on the material's intrinsic permeability to oxygen rather than on a pore-mediated pathway.

Despite differences in membrane properties and transport mechanisms (Table 1), oxygenation efficiency was comparable across all membrane types. Although NPSiN was expected to outperform PP and PDMS due to its ultra-high permeability, experimental results showed no significant differences (Fig. 3a and b, $p > 0.05$). The rate-limiting steps in oxygen transfer appear to be governed by processes on the blood side. This finding was further supported by the observed oxygen transport performance of a hypothetical infinitely permeable membrane. Even with perfect oxygen transfer efficiency of the membrane, the oxygen increase remained essentially the same as that achieved with the three tested membranes (Fig. 3e and f).
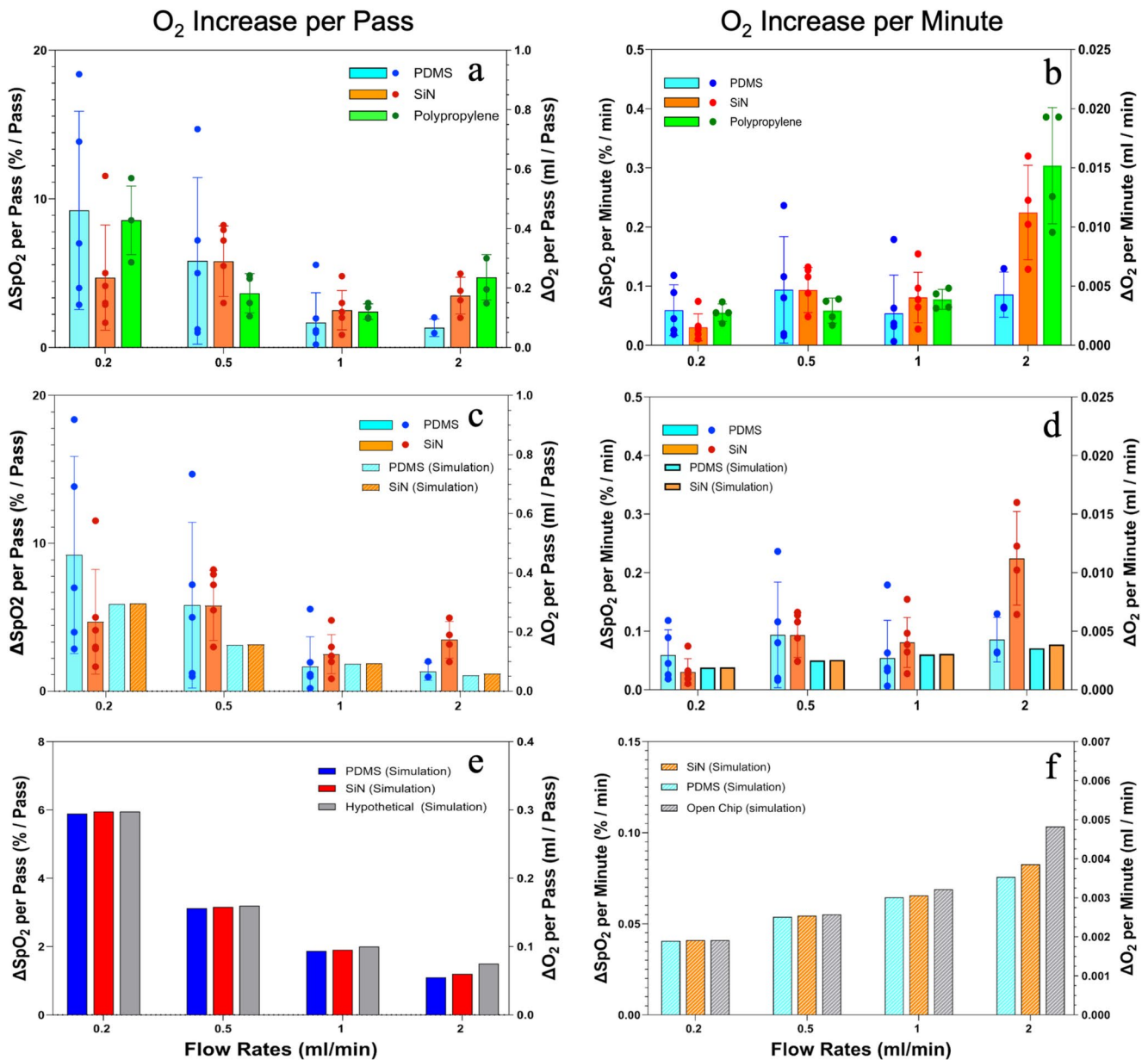
Fig. 3 Δ SpO$_2$ (%) and Δ O$_2$ (ml) of blood for different membranes at different flow rates, (**a**) per-pass (empirical: PDMS, SiN, and Polypropylene), (**b**) per-minute (empirical: PDMS, SiN, and Polypropylene), (**c**) per-pass (empirical and simulation: PDMS and SiN), (**d**) per-min- ute (empirical and simulation: PDMS and SiN), (**e**) per-pass (simulation: PDMS, SiN, and Hypothetical), (**f**) per-minute ((simulation: PDMS, SiN, and Hypothetical). In each panel, the left y-axis shows Δ SpO$_2$ (%) and the right y-axis shows Δ O$_2$ (ml)

As illustrated in Fig. 3a and c, oxygen transport per-pass decreases as flow rate increases due to reduced residence time of blood adjacent to the oxygenating membrane. At lower flow rates, prolonged membrane contact allows more complete oxygen diffusion, with residence times of approximately 47.5, 19, 9.5, and 4.75 s at flow rates of 0.2, 0.5, 1, and 2 mL/min, respectively. Higher flow rates reduce equilibration time, diminishing per-pass oxygen gain; however, total oxygen delivery per unit time may increase (Fig. 3b and d) as more blood volume is processed per time.

The movement of oxygen within the ECMO system is comprised of several steps: first, oxygen moves across the membrane (through pore-mediated diffusion or diffusion through non-porous membrane material); second, it diffuses through the blood plasma; third, it diffuses through red blood cells (RBCs) membrane, where it eventually binds to hemoglobin. While each step plays a role, the overall rate of oxygen uptake is dictated by the slowest, rate-limiting, step. Plasma diffusion resistance can be estimated by assuming a typical distance oxygen travels (Δx_{plasma}) as half the channel height. Given the oxygen diffusion coefficient in plasma,

$D_{plasma} = 1.62 \times 10^{-9}$ m²/s, the plasma diffusion resistance is, $R_{plasma} = \Delta x_{plasma} / D_{plasma} \approx 123,500$ s/m. Similarly, R_{rbc} is estimated as 2,000 s/m assuming RBC membrane thickness, $t_{rbc} \approx 10$ nm, and diffusion coefficient of oxygen in RBC membrane, $D_{rbc} = 5 \times 10^{-12}$ m²/s (Moll 1969). Assuming oxygen binding resistance to hemoglobin is negligible, the total blood-side resistance sums to, $R_{total} = R_{plasma} + R_{rbc} = 125,500$ s/m and is dominated by the resistance of oxygen moving through the plasma. In comparison, the membrane resistance for NPSiN and PDMS is 2.8 s/m and 27,000 s/m respectively, assuming oxygen partial pressure difference (ΔP) is 120 mmHg. If the blood-side resistance (125,500 s/m) already limits how much oxygen can enter the RBCs, then making the significantly lower permeability of SiN provides only ~20% improvement in overall transfer as compared to PDMS because diffusive transport through the plasma is the dominant resistance. Under the tested flow rates (0.2, 0.5, 1, 2 ml/min) the differences in membrane resistance does not materially impact net oxygen uptake, as transport is still limited by the larger blood-side resistance.

To confirm the dominant effect of the plasma resistance, we conducted a membrane transport experiment using two PDMS membranes of differing thicknesses (20 μm and 200 μm). In this setup, water was used in place of blood, while all other experimental parameters were held constant. For both membrane thicknesses, we measured the change in oxygen at two different water flow rates. Notably, despite the membranes exhibiting an order-of-magnitude difference in oxygen permeability, the measured oxygen transport did not change significantly (Fig. S3). These findings are consistent with the trends observed in Fig. 3 and further substantiate that the dominant resistance to oxygen transfer resides on in the blood side of the device and a result of the diffusion through the plasma, rather than in the membrane itself. This supports the conclusion that, under certain operating conditions, membrane resistance may be negligible relative to blood-side transport limitations.

The similarity in oxygen transport observed among NPSiN, PP, and PDMS membrane devices suggests that optimizing ECMO oxygenation in microfluidic systems may benefit more from addressing the blood-side limitations rather than from selecting membrane materials solely based on gas permeability. For instance, the introduction of mixing elements in the blood side geometry that enhances mixing, could potentially have a greater impact on oxygen transfer efficiency than membrane material changes. Our findings may indicated the need for a paradigm shift in ECMO design for microfluidic systems, focusing on blood-side flow enhancement to overcome diffusion and binding limitations.

Although membrane material does not govern oxygen transfer efficiency in microfluidic ECMO systems in the conditions that we tested, its importance in other applications remains an area of ongoing investigation. Urea has a diffusion coefficient of approximately 1.382×10^{-5} cm²/s at 25 °C (Winkelmann 2018), comparable to that of oxygen. In dialysis, urea diffuses across the membrane due to a concentration gradient. A seminal study by Hill et al. demonstrated that a nanoporous SiN membrane in a microfluidic dialysis device offers improvements over conventional dialysis membranes for a 300 μl/min flow rate (Hill et al. 2020). They showed that nanoporous SiN membranes achieved area-normalized clearance of up to 60,000 mL min^{-1}m^{-2} for small solutes—more than 50× higher than the ~1,000 mL min^{-1}m^{-2} typical of commercial polysulfone (PSU) and cellulose triacetate (CTA) membrane dialyzers. In a uremic rat model, 110 mm² of NPN-O (nanoporous membrane) lowered serum urea by 26% in 4 h, whereas conventional membranes with ~220 mm² area had no measurable effect.

To summarize, while membrane material is not the primary factor in blood oxygenation due to the presence of other significant resistances, such as oxygen diffusion rate in plasma, it may become crucial in applications where the membrane itself is the dominant resistance to transport, whether the result of different molecule or different device geometry. This distinction highlights the need to consider the relative contributions of various resistances when selecting membrane materials.

We acknowledge that flow rates of 0.2–2 mL/min are lower than typical clinical flows in ECMO settings. Our present aim is to characterize and compare membrane performance under controlled microfluidic conditions, not to design a clinical device. Transport scales with membrane area and future design work that involves device scaling, stacking, and iterative design improvements would be required to bridge the gap to physiologically relevant flow rates. We believe these initial findings serve as an important foundation for subsequent scale-up efforts.

The results of this study should be considered with an understanding of potential influences from the experimental setup and materials used. First, the variability in blood samples, such as donor-to-donor or species-to-species differences in hemoglobin concentration and overall blood composition, could impact oxygen transport performance. To minimize the influence of blood variability, all membranes tested on a given day were evaluated using the same lot of blood. Despite this control, some day-to-day variability remained, which is reflected in the scatter of the data points shown in Fig. 3. Second, the flow rates selected for the experiments, while representative of microfluidic ECMO applications, may not encompass all physiological or clinical conditions. Higher or lower flow rates could alter RBC residence times and mixing dynamics, potentially affecting oxygen transfer performance. Finally, the geometry of the

device, including channel dimensions and membrane placement, may play a critical role in determining flow patterns and oxygen transport. Different geometrical configurations may yield varied oxygenation results, making it essential to consider these design factors when extrapolating the findings to broader ECMO applications. Our findings remain robust within the tested conditions, but these limitations emphasize the need for additional studies that explore a wider range of flow rates, device geometries, and blood characteristics to generalize conclusions.

Declarations

Competing interests The authors declare no competing interests.

References

E.N. Abada, B.J. Feinberg, S. Roy, Biomed. Microdevices. **20**, 86 (2018)

M. Abudupataer, N. Chen, S. Yan, F. Alam, Y. Shi, L. Wang, H. Lai, J. Li, K. Zhu, C. Wang, Biomed. Microdevices. **22**, 10 (2020)

M. Ariyoshi, S. Fujikawa, T. Kunitake, ACS Appl. Mater. Interfaces. **13**, 61189 (2021)

C. Aubron, A.C. Cheng, D. Pilcher, T. Leong, G. Magrin, D.J. Cooper, C. Scheinkestel, V. Pellegrino, Crit. Care. **17**, R73 (2013)

S.C. Auld, M. Caridi-Scheible, J.M. Blum, C. Robichaux, C. Kraft, J.T. Jacob, C.S. Jabaley, D. Carpenter, R. Kaplow, A.C. Hernandez-Romieu, M.W. Adelman, G.S. Martin, C.M. Coopersmith, D.J. Murphy, Crit. Care Med. **48**, e799 (2020)

D.A. Berlin, R.M. Gulick, F.J. Martinez, N. Engl. J. Med. **383**, 2451 (2020)

D.G. Blauvelt, B.W. Chui, N.C. Higgins, F.J. Baltazar, S. Roy, Biomed. Microdevices. **25**, 2 (2023)

K.A. Burgess, H.-H. Hu, W.R. Wagner, W.J. Federspiel, Biomed. Microdevices. **11**, 117 (2009)

B. Chui, D. Blauvelt, F. Baltazar, T. Haniff, J. Moyer, N. Higgins, P. Oishi, S. Roy, *2022 Solid-State, Actuators, and Microsystems Workshop Technical Digest* (Transducer Research Foundation, San Diego, 2022), pp. 272–273

A.T. Conlisk, S. Datta, W.H. Fissell, S. Roy, Ann. Biomed. Eng. **37**, 722 (2009)

M. Dabaghi, G. Fusch, N. Saraei, N. Rochow, J.L. Brash, C. Fusch, P Ravi Selvaganapathy Biomicrofluidics. **12**, 44101 (2018a)

M. Dabaghi, N. Saraei, G. Fusch, N. Rochow, J.L. Brash, C. Fusch, P.R. Selvaganapathy, Lab. Chip. **18**, 3780 (2018b)

M. Dabaghi, N. Saraei, G. Fusch, N. Rochow, J.L. Brash, C. Fusch, P. Ravi Selvaganapathy, Biomicrofluidics **13**, (2019)

T.A. Desai, D.J. Hansford, L. Kulinsky, A.H. Nashat, G. Rasi, J. Tu, Y. Wang, M. Zhang, M. Ferrari, Biomed. Microdevices. **2**, 11 (1999)

E. Fan, D. Brodie, A.S. Slutsky, Am. J. Respir Crit. Care Med. **195**, 1137 (2017)

F. Formica, L. Avalli, A. Martino, E. Maggioni, M. Muratore, O. Ferro, A. Pesenti, G. Paolini, ASAIO J. **54**, 89 (2008)

A.A. Gimbel, J.C. Hsiao, E.S. Kim, D.J. Lewis, T.F. Risoleo, J.N. Urban, J.T. Borenstein, Artif. Organs. **45**, E247 (2021)

B. Gimi, J. Kwon, J. Liu, Y. Su, K. Nemani, K. Trivedi, Y. Cui, B. Vachha, R. Mason, W. Hu, J.-B. Lee, Biomed. Microdevices. **11**, 1205 (2009)

J. Han, J. Fu, R.B. Schoch, Lab. Chip. **8**, 23 (2008a)

J. Han, J. Fu, R.B. Schoch, Lab. Chip. **8**, 23 (2008b)

F. Haque, J. Li, H.-C. Wu, X.-J. Liang, P. Guo, Nano Today. **8**, 56 (2013)

A.V. Hill, J. Physiol. **40**, 4 (1910)

K. Hill, S.N. Walker, A. Salminen, H.L. Chung, X. Li, B. Ezzat, J.J. Miller, J.S. DesOrmeaux, J. Zhang, A. Hayden, T. Burgin, L. Piraino, M.N. May, T.R. Gaborski, J.A. Roussie, J. Taylor, L. DiVincenti, A.A. Shestopalov, J.L. McGrath, D.G. Johnson, Adv. Healthc. Mater. **9**, (2020)

H. Hou, N. Khan, S. Gohain, M.L. Kuppusamy, P. Kuppusamy, Biomed. Microdevices. **20**, 29 (2018)

N. Imtiaz, W.A. Stoddard, A.T. Johnson, C.R. Amato, J.A. Carter, J.A. Roussie, S.W. Day, ASAIO J. **68**, 87 (2022)

N. Imtiaz, W.A. Stoddard, J.A. Carter, J. Roussie, S. Day, ASAIO J. **69**, 93 (2023a)

N. Imtiaz, T. Siam, Siam, CFD Lett. **15**, 45 (2023b)

N. Imtiaz, M.D. Poskus, W.A. Stoddard, T.R. Gaborski, S.W. Day, Micromachines (Basel). **15**, 790 (2024)

G. Jeon, S.Y. Yang, J.K. Kim, J. Mater. Chem. **22**, 14814 (2012)

E. Kim, H. Xiong, C.C. Striemer, D.Z. Fang, P.M. Fauchet, J.L. McGrath, S. Amemiya, J. Am. Chem. Soc. **130**, 4230 (2008)

X. Li, Z. Guo, B. Li, X. Zhang, R. Tian, W. Wu, Z. Zhang, Y. Lu, N. Chen, S.P. Clifford, J. Huang, ASAIO J. **66**, 475 (2020)

L.J. Ma, E.A. Akor, A.J. Thompson, J.A. Potkay, Micromachines (Basel) **13**, 822 (2022). https://doi.org/10.3390/mi13060822

J.J. Miller, J.A. Carter, K. Hill, J.-P.S. DesOrmeaux, R.N. Carter, T.R. Gaborski, J.A. Roussie, J.L. McGrath, D.G. Johnson, Membr. (Basel). **10**, 119 (2020)

W. Moll, Pflügers Archiv Eur. J. Physiol. **305**, 269 (1969)

M.F. Odish, P.S. Garimella, H. Crisostomo, C. Yi, R.L. Owens, T. Pollema, ASAIO J. **69**, e455 (2023)

J.A. Potkay, Lab Chip **14**, 4122 (2014). https://doi.org/10.1039/c4lc00828f

C. Qi, C.C. Striemer, T.R. Gaborski, J.L. McGrath, P.M. Fauchet, Small. **10**, 2946 (2014)

T.R. Roberts, A. Persello, G.T. Harea, E.M. Vedula, B.C. Isenberg, Y. Zang, J. Santos, J.T. Borenstein, A.I. Batchinsky, ASAIO J. (2024)

R.P. Rode, H.H. Chung, H.N. Miller, T.R. Gaborski, S. Moghaddam, BioRxiv 2020.05.26.116863 (2020)

J. Santos, E.M. Vedula, W. Lai, B.C. Isenberg, D.J. Lewis, D. Lang, D. Sutherland, T. R. https://doi.org/10.3390/mi12080888

S. Shin, U. Nasim, H. O'Connor, Y. Hong, Curr. Opin. Organ. Transpl. **29**, 349 (2024)

Z. Siwy, I.D. Kosińska, A. Fuliński, C.R. Martin, Phys. Rev. Lett. **94**, 048102 (2005)

J.L. Snyder, A. Clark, D.Z. Fang, T.R. Gaborski, C.C. Striemer, P.M. Fauchet, J.L. McGrath, J. Memb. Sci. **369**, 119 (2011)

R.J. Sové, G.M. Fraser, D. Goldman, C.G. Ellis, PLoS One. **11**, e0166289 (2016)

P. Stroeve, N. Ileri, Trends Biotechnol. **29**, 259 (2011)

N. Valenzuela-Faccini, C. Poveda-Henao, C. Flórez-Navas, M. Pérez-Garzón, N. Boada-Becerra, M. Mercado-Diaz, P. Salcedo, H. Robayo-Amortegui, BMC Pulm Med. **24**, 41 (2024)

J.W.H. Walker, Clinical Methods: The History, Physical, and Laboratory Examinations. (1990)

J. Winkelmann, *Diffusion in Gases, Liquids and Electrolytes* (Springer Berlin Heidelberg, Berlin, Heidelberg, 2018), pp. 111–113

E. Wright, J.J. Miller, M. Csordas, A.R. Gosselin, J.A. Carter, J.L. McGrath, D.R. Latulippe, J.A. Roussie, Biotechnol. Bioeng. **117**, 879 (2020)